Simulating Quantum Many-Body Dynamics On A Current Digital Quantum Computer

Aaron Anhalt, Matriculation No.: 03716328
David Zambrano, Matriculation No.: 03768441
Ruben Wernadorfer, Matriculation No.: 03711473

Supervised by
Prof. Dr. Michael Knap

January 9, 2025

Table of Contents

1   Introduction

Quantum computing represents a paradigm shift from classical computing by leveraging the principles of quantum mechanics, such as superposition and entanglement, to perform computations. Unlike classical bits, quantum bits (qubits) can exist in multiple states simultaneously, offering the potential for vastly increased computational power. Over the past few decades, significant progress has been made towards realizing practical quantum computers, with various platforms, including cold atoms, trapped ions, and superconducting qubits, demonstrating capabilities for universal computation.

Among these, superconducting qubits have emerged as a leading candidate due to their scalability and flexibility. These qubits are based on the architecture known as circuit quantum electrodynamics (cQED) and are constructed from superconducting materials that form circuits with inductors, capacitors, and Josephson junctions. The energy levels in these circuits are manipulated using microwave pulses to perform quantum gates, which are essential for quantum computation. One of the most notable milestones in this field was Google's claim of quantum supremacy in 2019 using a 53-qubit superconducting processor, Sycamore.

In this practical training, participants will delve into quantum computation using the Qiskit library to program superconducting quantum computers. The training is divided into two parts: Day 1 (Chapters 1-6) focuses on the basics of quantum computation and Qiskit installation, while Day 2 (Chapters 7-9) applies these concepts to a many-body system, specifically the transverse field Ising model. We simulated quantum circuits to understand phenomena like Dynamical Quantum Phase Transitions (DQPTs) and extract observables such as magnetization and entanglement dynamics.

This hands-on approach aims to provide a comprehensive understanding of both the theoretical and practical aspects of quantum computing.

2 Error-Mitigation on NISQ Devices

On NISQ devices, fully error corrected quantum algorithms are not implementable, because the overhead of gates to correct for errors introduces introduces more error itself, and is not feasible yet to be fabricated due to e.g. limited chip space or control and readout lines. Therefore, in current devices, various protocols to mitigate errors have been brought forth. In this practical, we focus on the readout matrix unfolding protocol, a straight forward approach to mitigate readout error. The readout of superconducting qubit is performed by the interaction with a passing microwave and the consequent measurement of the returned signal. Errors occur due to possible decay or excitation during the measurement process or due to insufficient separation of the measured states in the return signal, compared to the spread of the result.

The first step of this protocol is the calibration, that is performed on an N qubit device by preparing all 2^N basis states and measuring them on all N qubits. Each state is prepared and measured m times. The calibration effort consists then of $m2^N$ measurements, making it less feasible for large numbers of qubits. The calibration results in the matrix of probabilities

$$P_{ab} = \Pr(\text{Measured bit string} \mid \text{Prepared bit string } b), \tag{2.1}$$

which contains the information about the systematic errors made in the readout (but also the errors in state preparation).

The foundational assumption of the mitigation step is, that a a vector of actual state probabilities v is reproducibly converted to a vector of measurement probabilities v' in the process, as indicated by the probability matrix P:

$$v'_a = \sum_b P_{ab} v_b. \tag{2.2}$$

In the actual quantum calculations, measured result vector v' is obtained by averaging of many shots, v'_a is then the probability to measure the state bit string labeled a. The reconstructed calculation $\tilde{v}$ result can simply be obtained by multiplying the measurement result with the inverse of the probability matrix, and corresponds to the actual calculation result to the same extent as the assumption 2.2 holds.

$$\tilde{v}_a = \sum_{a'} P^{-1}_{aa'} v'_{a'} \tag{2.3}$$

$$= \sum_{a'} P^{-1}_{aa'} \sum_b P_{a'b} v_b \tag{2.4}$$

$$= v_b \quad \text{with} \sum_{a'} P^{-1}_{aa'} \sum_b P_{a'b} = 1\!\!1_{ab} \tag{2.5}$$

In reality, $\tilde{v}$ can become unphysical, because P just mirrors a statistical process. This can be helped by introducing constraints to the solving of 2.2.

Keeping in mind, that v' is an actually measured probability distribution, we know that $\sum_a (v'_a)! = 1$. Combining this with the assumption in 2.2, we can show, that the inverted $\tilde{v}$

fulfills the probability summation condition as well:

$$\sum_a (v'_a) = 1 = \sum_a \sum_b P_{ab} v_b \qquad (2.6)$$

$$= \sum_b \sum_a P_{ab} v_b \qquad (2.7)$$

$$\qquad (2.8)$$

The probability of measuring the prepared bit string b in any result a is 100%, therefore $\sum_a P_{ab} = 1$. And consequently:

$$\sum_b v_b = 1 \qquad (2.9)$$

3 Quantum Teleportation

Quantum teleportation is a technique used to transmit (teleport) any quantum state between two observers (here named Alice and Bob), given they share a maximally entangled two-qubit state, also known as a bell state. The circuits to produce all four bell states starting from the $|00\rangle$ state are shown in Figure 3.1.

(a) Circuit to construct the $|\Phi^+\rangle = \frac{1}{\sqrt{2}}(|00\rangle + |11\rangle)$ state.

(b) Circuit to construct the $|\Phi^-\rangle = \frac{1}{\sqrt{2}}(|00\rangle - |11\rangle)$ state.

(c) Circuit to construct the $|\psi^+\rangle = \frac{1}{\sqrt{2}}(|01\rangle + |10\rangle)$ state.

(d) Circuit to construct the $|\psi^-\rangle = \frac{1}{\sqrt{2}}(|01\rangle - |01\rangle)$ state.
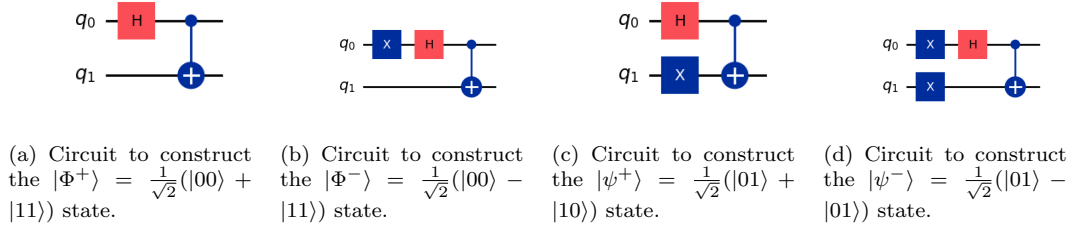
Figure 3.1: Circuits to produce all 4 bell states.

The observer sending the state, in this case, Alice, will also need to perform a bell measurement on the qubit that will be teleported and her qubit that forms part of the shared bell state. This is accomplished by using a CNOT gate, which uses the state to be teleported as the control qubit, followed by a Hadamard gate on that same qubit. Then, both registries are measured, and the four results correspond to the different bell state measurements. The first part of the teleportation protocol would consist of generating a bell state between Alice and Bob, then setting up the bell measurement with a CNOt gate and a Hadamard gate between the quantum register holding the state we want to teleport and Alice. Up to this point, the joint quantum state between all three systems would look like this:

$$
\begin{aligned}
&|\Phi^+\rangle_{SA} \left(\alpha |0\rangle_B + \beta |1\rangle_B\right) + |\Phi^-\rangle_{SA} \left(\alpha |0\rangle_B - \beta |1\rangle_B\right) \\
&+ |\Psi^+\rangle_{SA} \left(\alpha |1\rangle_B + \beta |0\rangle_B\right) + |\Psi^-\rangle_{SA} \left(\alpha |1\rangle_B - \beta |0\rangle_B\right)
\end{aligned} \tag{3.1}
$$

Depending on the result of the bell measurement on both Alice´s qubits, Bob's state will collapse into one of four states. Once Alice has the result of the measurement, she can communicate it to Bob so he knows which gate to apply on his qubit to obtain the desired state. The possible outcomes relating the measurement of Alice´s qubits, the bell state obtained, and the operation to be performed by Bob are displayed in Table 3.1, and a complete circuit for the teleportation protocol is shown in Figure 3.2.

Measurement	Bell State	Unitary Operator
00	$|\Phi^+\rangle$	$\mathbf{1}$
01	$|\Phi^-\rangle$	σ_x
10	$|\psi^+\rangle$	σ_z
11	$|\psi^-\rangle$	$\sigma_z\sigma_x$

Table 3.1: Results for the bell measurements and the respective unitary operator needed to obtain the desired state in the teleportation protocol (assuming the initial shared bell state was $|\Phi^+\rangle$).
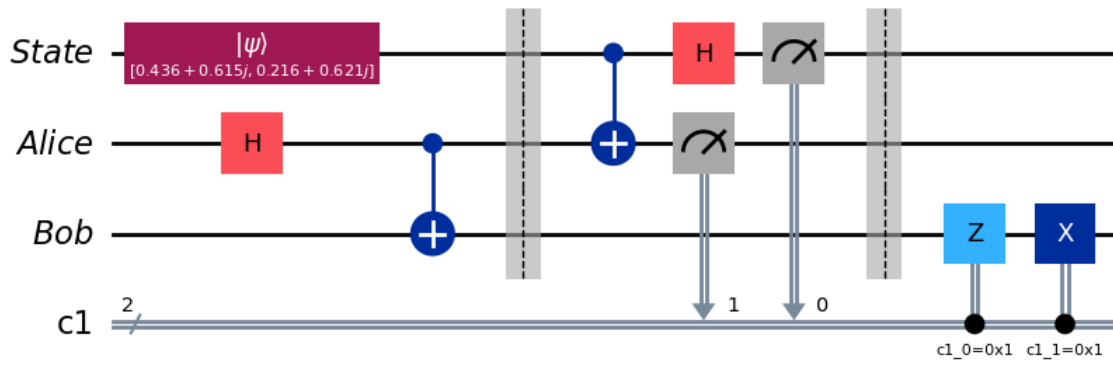

Figure 3.2: Complete quantum teleportation circuit. Barriers separate the creation of the bel state, bell measurement, and conditional gate operations.

4 Rabi Oscillations

The periodic transition between two states of a quantum System in the presence of a periodic driving field is called Rabi oscillation. They are a key component to implement single qubit gates. The Hamiltonian describing system is

$$\hat{H} = -\frac{\omega_0}{2}\hat{\sigma}_z + \omega_1 \cos(\omega t)\hat{\sigma}_x. \tag{4.1}$$

In the example of a two-level spin system, the first part would correspond to a static magnetic field applied in z-direction $\mathbf{B}_z = \frac{\omega_0}{\gamma}\,\hat{z}$ and the second part constitutes the transversal driving field $\mathbf{B}_x = \frac{\omega_1}{\gamma}\cos(\omega t)\hat{x}$ with frequency $\frac{\omega}{2\pi}$. The evolution of the state $\psi(t) = \alpha(t)\left|0\right\rangle + \beta(t)\left|1\right\rangle$ can be analytically calculated by applying the rotating wave approximation (valid for weak drives close to resonance $\omega_1 << \omega_0$, $\omega - \omega_0 << \omega + \omega_0$).
Initializing the ground state $\left|0\right\rangle$, state coefficients evolve like this:

$$\alpha(t) = e^{i\omega t/2}\left(\cos\left(\frac{\Omega t}{2}\right) - \frac{i\Delta}{\Omega}\sin\left(\frac{\Omega t}{2}\right)\right)$$

$$\beta(t) = -e^{-i\omega t/2}\frac{i\omega_1}{\Omega}\sin\left(\frac{\Omega t}{2}\right) \tag{4.2}$$

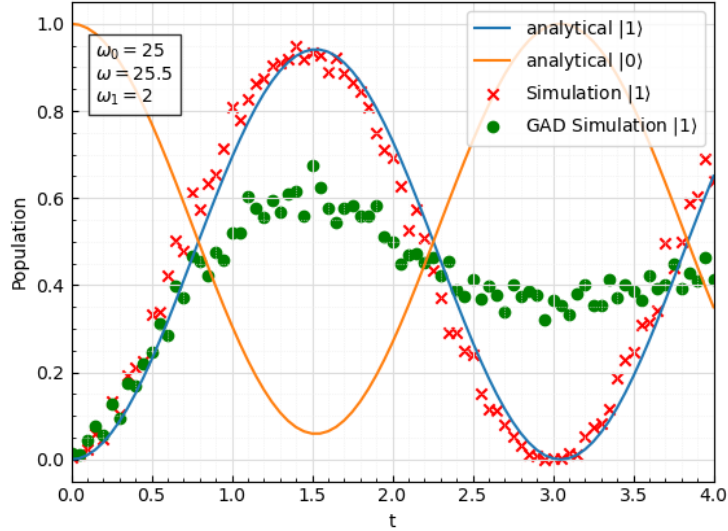where $\Delta = \omega - \omega_0$ and $\Omega = \sqrt{\omega_1^2 + \Delta^2}$.

Figure 4.1: Analytical evolution (RWA) of the the state population with a slightly off-resonant drive (solid lines), trotterized quantum simulation without (red) and with (green) GAD errors.

This time evolution can also be approximated by a quantum simulation, using the time-dependent Trotterization

$$\hat{U}(t) = \mathcal{T}e^{-i\int_0^t \hat{H}(t)dt} \tag{4.3}$$

$$\approx \prod_{n=0}^{N-1} e^{-i\hat{H}(n\delta t)\delta t} \tag{4.4}$$

$$\approx \prod_{n=0}^{N-1} e^{\frac{i\omega_0\delta t}{2}\hat{\sigma}_z} e^{-i\omega_1\delta t\cos(\omega n\delta t)\hat{\sigma}_x} \tag{4.5}$$

Which splits the time interval in to N equal parts and assumes $\hat{H}$ to be constant during each time interval of length $\delta t = t/N$. The second step splits the Hamiltonian in it's components, neglecting that they don't commute.

The Trotterized version corresponds to a successive application of R_z and R_x, which we can implement on a digital quantum computer. We simulate this with Qiskit.

If the Trotterized evolution is calculated on an actual quantum computer, there will be noise from unwanted interaction with the environment, that degrades the result. We mimic this in Qiskit by implementing a generalized amplitude damping quantum channel (GAD) in our simulation as follows: Noise can be depicted by a quantum channel

$$\Lambda(\rho) = \sum_{i=0}^{3} E_i\rho E_i^{\dagger}, \tag{4.6}$$

which is applied to the state after every single qubit gate.

When γ carries the information about the probability of a state excitation or decay and p is the expectation value of excitation for the thermal equilibrium sate, the amplitude damping channel is parameterized by these operators:

$$E_0 = \sqrt{1-p}\begin{bmatrix}1 & 0 \\ 0 & \sqrt{1-\gamma}\end{bmatrix}, \quad E_1 = \sqrt{1-p}\begin{bmatrix}0 & \sqrt{\gamma} \\ 0 & 0\end{bmatrix}$$
$$E_2 = \sqrt{p}\begin{bmatrix}\sqrt{1-\gamma} & 0 \\ 0 & 1\end{bmatrix}, \qquad E_3 = \sqrt{p}\begin{bmatrix}0 & 0 \\ \sqrt{\gamma} & 0\end{bmatrix}. \tag{4.7}$$

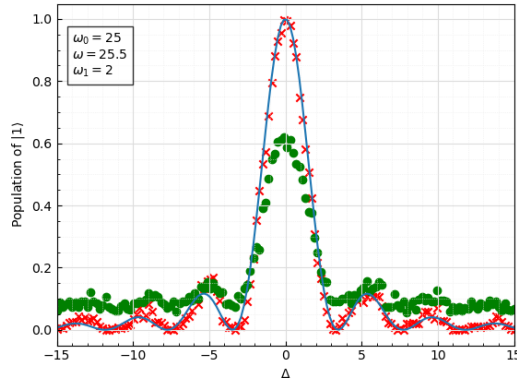If not stated otherwise, we will use the noise parameters $\gamma = 0.02$ and $p = 0.1$.

Figure 4.2: Maximally achievable $|1\rangle$-state population after $t = \pi/\omega_1$.

In 4.1 the good alignment of the Trotterization and the RWA is shown. With the given noise parameters, a significant damping and quick loss of information can be observed. Similar results can be observed in 4.2, where
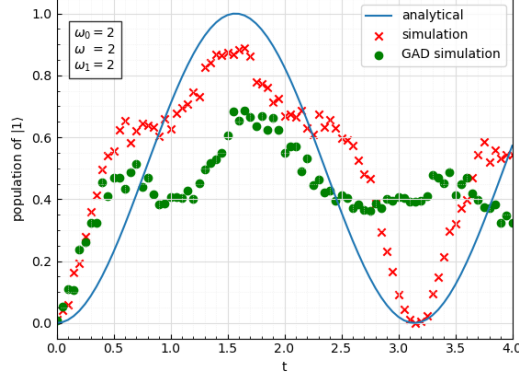
7

Figure 4.3: Deviation of analytical (RWA) approximation (blue line) to trotterized simulation with and without error.

The break-down of the rotating wave approximation for a strong drive ($\mathbb{O}(\omega_0) \approx \mathbb{O}(\omega_1)$) becomes visible in 4.3: Higher order features - at higher frequencies - gain a relevant influence but are not represented in the analytical approximations.
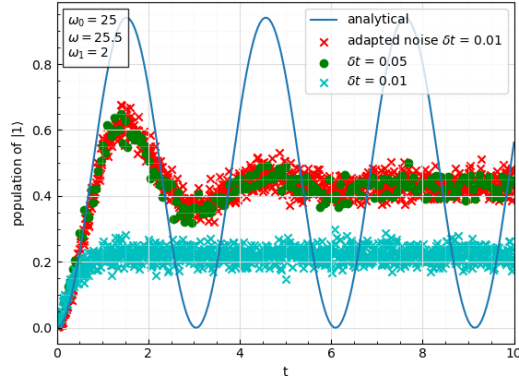

Figure 4.4: Decay simulation compared for different time step lengths δt. If no noise adaptation is attempted (cyan), only the decay to the thermal population is observed. If the noise amplitude is adapted to the number of gates (red) the results are comparable to the results for the original time step (green) and closer to the ideal analytical solution (blue).

The accuracy of the Trotterization depends on the length of the time steps. When the length is reduced to a fifth of the previous step length, the GAD simulation has to be adapted as well. The corresponding simulations are seen in 4.4 If the same noise channel is applied after every gate, the noise scales with increasing number of steps. A quick decay to the thermal state of the two-level is observed before any other feature of the evolution can be seen. When the decay probability is reduced with the same factor as the number of gates increases $\gamma \to \frac{1}{5}\gamma$, a the result agrees with the large time step. It is therefore confirmed, that the original time step was (at least in the scope that we consider), small enough to achieve reliable results. Furthermore, this indicates, that Trotterized quantum simulations have to make a trade-off between the approximation error by large time steps and the noise error added by every additional step.

Investigating the decay more thoroughly, we recognize the competition of two processes: the decay to the equilibrium state and the excitation by the drive. In 4.5 we compare the
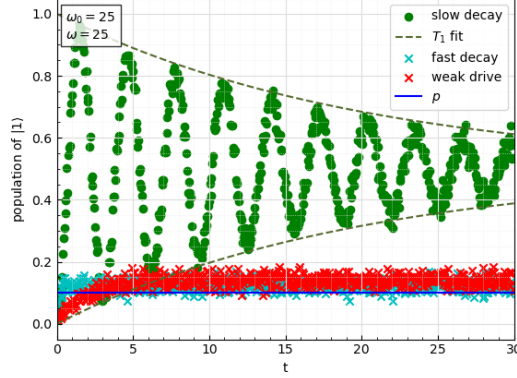
Figure 4.5: Noise influence at resonant driving: simulation of reduced decay probability $\gamma = 0.002$, $\omega_1 = 2$ (green dots) with a fit of the exponential decay with $T_1 = 20$ (green dashed line). Simulations for fast decay ($\gamma = 0.2$, $\omega_1 = 2$) (cyan) and weak drive ($\omega_1 = 0.2$, $\gamma = 0.02$) with decay towards the equilibrium population $p = 0.1$ (solid blue line).

noisy state evolution for resonant driving ($\omega = \omega_0 = 25$) and observe the two domains. If the drive is dominating ($\omega = 2$, $\gamma = 0.01$, we see the typical exponential decay of Rabi Oscillations to the completely mixed state ($\rho = \frac{1}{2}\mathbb{I}$. Over the course of the experiment, a decay or excitation happens, introducing a random shift in the oscillation process.

In the case of weak driving (low ω_1) and the case of very fast decay, the equilibrium state with a population of $\langle 1| \rho |1\rangle = p = 0.1$ is approached, with a slight shift towards the mixed state, that is introduced by the drive. The decay is so fast, that in before a noticeable oscillation can happen, the state decays.
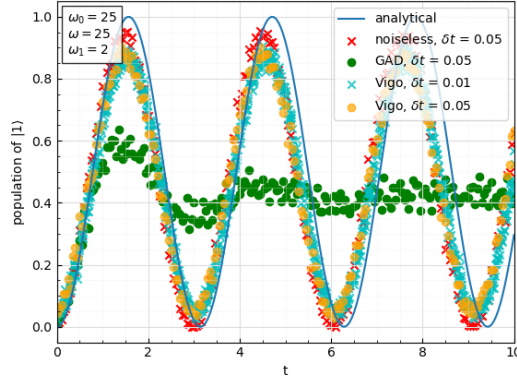

Figure 4.6: Comparison of GAD simulation ($\gamma = 0.02$, $p = 0.1$) (green) with a realistic quantum noise back-end (Vigo) (orange). The increase of the number of gates (cyan) does not show a relevant noise effect in this scope. The RWA analytical solution (blue) and a noiseless Trotter approximation (red) are shown for reference.

Lastly, we want to compare our noise investigation to the realistic noise in a quantum device. In the previous examples, the GAD noise that we implemented posed serious limitations to the number of gates after which the obtained results are still meaningful.

In 4.6, we use a fake machine back-end provided by Qiskit, that implements more realistic noise behavior from the "Vigo" device. It becomes apparent, that the realistic noise model reproduces the expected analytical results faithfully on much larger scales and doesn't even

suffer from the increase of the number of gates for reducing the time step length. The noise deviation around the maxima and minima of the population oscillation, which doesn't increase much over time hints at a readout error, that could be further improved by implementing readout error mitigation as explained in 2.

5 Single-qubit Tomography

When measuring populations in quantum states, distinct states can yield identical results despite representing different physical scenarios. For example, measurements on $|0\rangle\langle 0| + |1\rangle\langle 1|$ and $|\psi\rangle\langle\psi|$ with $|\psi\rangle = \frac{1}{\sqrt{2}}(|0\rangle + |1\rangle)$ produce the same result, though the former is a statistical ensemble and the latter a pure state. Quantum State Tomography distinguishes quantum states by reconstructing their density matrices, which differ for distinct physical scenarios. A density matrix ρ can be expressed using Pauli matrices as

$$\rho = \sum_{i=0}^{3} c_i \hat{\sigma}_i. \tag{5.1}$$

The coefficients c_i are obtained via expectation values of Pauli operators:

$$c_i = \frac{1}{2}\langle\hat{\sigma}_i\rangle = \frac{1}{2}\text{Tr}(\hat{\sigma}_i\rho). \tag{5.2}$$

Here, $c_0 = \frac{1}{2}$, as $\hat{\sigma}_0$ is the identity matrix and any physical quantum state has unit trace. Finally, the fidelity between two quantum states, indicating their agreement, is defined as

$$F(\rho, \sigma) = \text{Tr}\left[\sqrt{\sqrt{\sigma}\rho\sqrt{\sigma}}\right]^2. \tag{5.3}$$

In the current setup, only population measurements are possible. To measure a different component (e.g., other than the z-component), it is necessary to rotate the quantum state before the measurement. The following identities illustrate how this can be achieved:

$$\begin{aligned}
HZH &= \frac{1}{2}\begin{pmatrix} 1 & 1 \\ 1 & -1 \end{pmatrix}\begin{pmatrix} 1 & 0 \\ 0 & -1 \end{pmatrix}\begin{pmatrix} 1 & 1 \\ 1 & -1 \end{pmatrix} = \frac{1}{2}\begin{pmatrix} 1 & 1 \\ 1 & -1 \end{pmatrix}\begin{pmatrix} 1 & 1 \\ -1 & 1 \end{pmatrix} \\
&= \frac{1}{2}\begin{pmatrix} 0 & 2 \\ 2 & 0 \end{pmatrix} = \begin{pmatrix} 0 & 1 \\ 1 & 0 \end{pmatrix} = X.
\end{aligned} \tag{5.4}$$

Similarly, for Y:

$$\begin{aligned}
SHZHS^\dagger &= SXS^\dagger = \begin{pmatrix} 1 & 0 \\ 0 & i \end{pmatrix}\begin{pmatrix} 0 & 1 \\ 1 & 0 \end{pmatrix}\begin{pmatrix} 1 & 0 \\ 0 & -i \end{pmatrix} \\
&= \begin{pmatrix} 1 & 0 \\ 0 & i \end{pmatrix}\begin{pmatrix} 0 & -i \\ i & 0 \end{pmatrix} = \begin{pmatrix} 0 & -i \\ i & 0 \end{pmatrix} = Y.
\end{aligned} \tag{5.5}$$

These identities demonstrate how a Z operation can be transformed into X or Y operations. This property enables the measurement of all components of the density matrix for a given quantum state.

To apply State Tomography on a quantum computer, the qubit state's components must be measured. From equations 5.4 and 5.5, a Z operation can be transformed into X or Y

operations. To calculate $\langle \hat{\sigma}_x \rangle$ and $\langle \hat{\sigma}_y \rangle$, the eigenstates of X and Y are transformed into Z-eigenstates via unitary transformations H and $HS^\dagger$, respectively.

The tomography method reconstructs the state $|\psi\rangle = (|0\rangle + e^{i\pi/4}|1\rangle)/\sqrt{2} = TH|0\rangle$, with T adding a phase $e^{i\pi/4}$ to $|1\rangle$. The density matrix is

$$\rho_{|\psi\rangle} = |\psi\rangle\langle\psi| = \frac{1}{2} \begin{pmatrix} 1 & \frac{1-i}{\sqrt{2}} \\ \frac{1+i}{\sqrt{2}} & 1 \end{pmatrix} \approx \begin{pmatrix} 0.5 & 0.354 - i0.354 \\ 0.354 + i0.354 & 0.5 \end{pmatrix}. \tag{5.6}$$

Averaging over 500 measurements gives $c_x = 0.35825$, $c_y = 0.34878$, $c_z = -0.00189$, reconstructing the density matrix as

$$\rho_{\text{meas}} = \begin{pmatrix} 0.476 & 0.318 - 0.316i \\ 0.318 + 0.316i & 0.524 \end{pmatrix}. \tag{5.7}$$

This matches the expected matrix with a fidelity of $F = 0.948$. Using Qiskit's built-in 'StateTomography()', the reconstructed matrix is

$$\rho_{\text{built-in}} = \begin{pmatrix} 0.50778 & 0.34163 - 0.36499i \\ 0.34163 + 0.36499i & 0.49221 \end{pmatrix}, \tag{5.8}$$

achieving an even higher fidelity of $F = 0.999$.

After successfully reconstructing a quantum state via State Tomography and observing Rabi Oscillations, we combine these methods. The coefficients of the quantum state in a Rabi Oscillation are rewritten from equation 4.2 such that $\alpha(t)$ is real.

$$\alpha(t) = \sqrt{\cos^2\left(\frac{\Omega t}{2}\right) + \frac{\Delta^2}{\Omega^2}\sin^2\left(\frac{\Omega t}{2}\right)}$$

$$\beta(t) = \frac{e^{-i\omega t}\left(\frac{\omega_1}{2\Omega}\sin(\Omega t) + i\frac{\omega_1\Delta}{\Omega^2}\sin^2\left(\frac{\Omega t}{2}\right)\right)}{\sqrt{\cos^2\left(\frac{\Omega t}{2}\right) + \frac{\Delta^2}{\Omega^2}\sin^2\left(\frac{\Omega t}{2}\right)}}. \tag{5.9}$$

State Tomography provides the density matrix for each time step:

$$\rho_{\text{Rabi}} = \begin{pmatrix} |\alpha(t)|^2 & \alpha(t)\beta^*(t) \\ \alpha^*(t)\beta(t) & |\beta(t)|^2 \end{pmatrix}. \tag{5.10}$$

Here, $\alpha(t)$ is the square root of the upper-left entry in equation 5.10, and $\beta(t)$ is derived by dividing the lower-left entry by $\alpha(t)$. Figure 5.1 shows the time evolution of $\alpha(t)$ and $\beta(t)$ along with their theoretical expectation.
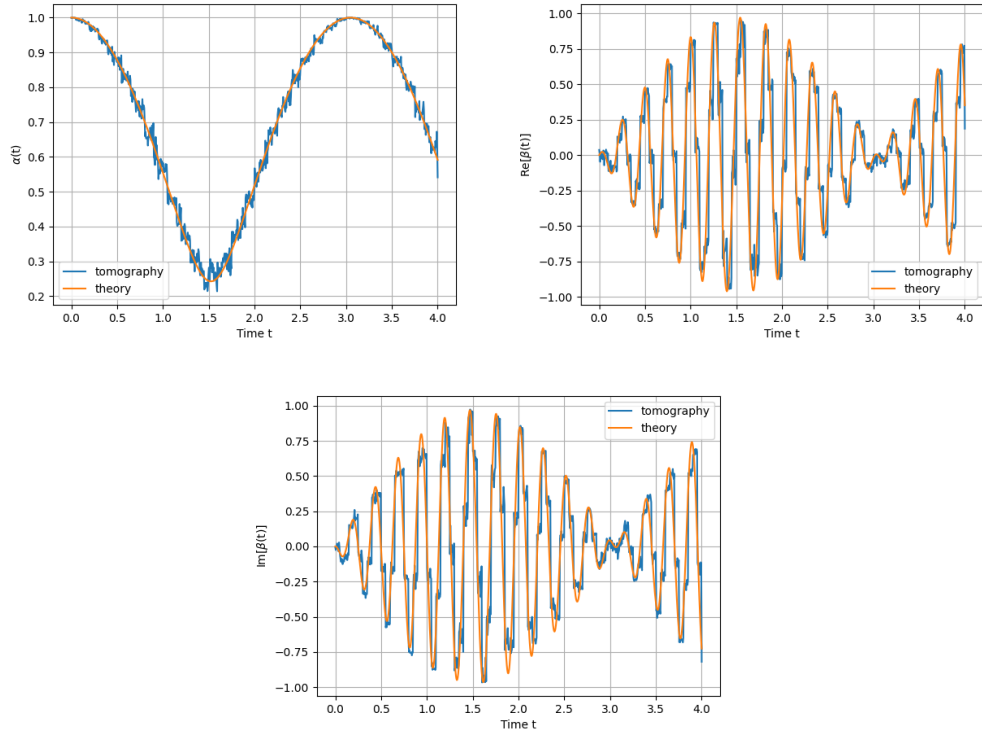
Figure 5.1: Coefficients (a) $\alpha(t)$, (b) Re[$\beta(t)$] and (c) Im[$\beta(t)$] of a Rabi Oscillation reconstructed by State Tomography. The coefficients show a real good agreement with the expected values from equation 5.9.

6 Variational Quantum Eigensolver

A promising application of near-term quantum computers in the study of quantum many-body systems is the Variational Quantum Eigensolver (VQE). The VQE is used to approximate the ground state of a local Hamiltonian $\hat{H}$ by employing the variational method. This method involves preparing a trial state $|\psi(\theta)\rangle$, which is parametrized by a set of parameters θ. The goal is to find the state that minimizes the energy $\langle\psi(\theta)|\hat{H}|\psi(\theta)\rangle$.

While evaluating $\langle\psi(\theta)|\hat{H}|\psi(\theta)\rangle$ for a given set of parameters θ is exponentially hard on classical computers for a general case of N qubits, the VQE leverages quantum computers to overcome this difficulty, Quantum computers can directly measure the energy expectation $\langle\psi(\theta)|\hat{H}|\psi(\theta)\rangle$ by measuring the expectation values of a list of Pauli strings that sum to $\hat{H}$. Thus, VQE is a quantum-classical hybrid algorithm where the quantum computer handles the challenging part of obtaining the expectation values, and the classical computer is responsible for the optimization of the parameters in the circuit.

In this section, we will apply the algorithm on a two-qubit system with the following hamiltonian:

$$\hat{H} = -\hat{\sigma}_x^1\hat{\sigma}_z^2 - \hat{\sigma}_z^1\hat{\sigma}_x^2 \tag{6.1}$$

And using the following trial state:

$$|\psi(a,b)\rangle = \exp\left(ia(\hat{\sigma}_z^1 + \hat{\sigma}_z^2)\right)\exp\left(ib(\hat{\sigma}_x^1\hat{\sigma}_z^2 + \hat{\sigma}_z^1\hat{\sigma}_x^2)\right)|00\rangle \tag{6.2}$$

To prepare the trial state, we used the circuit in Figure 6.1 with parameters { a, b } where the R_Z gate is a rotation around the z-axis on the Bloch sphere and the $R_{ZX}(\theta)$ gate is given by Equation 6.3.

$$R_{ZX}(\theta) = exp(-i\frac{\theta}{2}X \otimes Z) = \begin{bmatrix} \cos\frac{\theta}{2} & 0 & -i\sin\frac{\theta}{2} & 0 \\ 0 & \cos\frac{\theta}{2} & 0 & i\sin\frac{\theta}{2} \\ -i\sin\frac{\theta}{2} & 0 & \cos\frac{\theta}{2} & 0 \\ 0 & i\sin\frac{\theta}{2} & 0 & \cos\frac{\theta}{2} \end{bmatrix} \tag{6.3}$$
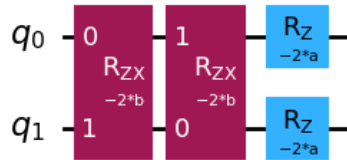

Figure 6.1: Parametrized quantum circuit for the trial state in Equation 6.2

For the classical optimization part, we run a grid search over the parameter space $a \in [0,\pi]$, $b \in [0,\pi]$, taking 20 equally spaced values for each parameter. The results of the grid

search are found on Figure 6.2a. The optimal parameters found were $a_{opt} = b_{opt} = 0.827$ and the respective expectation value is $E_{min} = -1.990$.
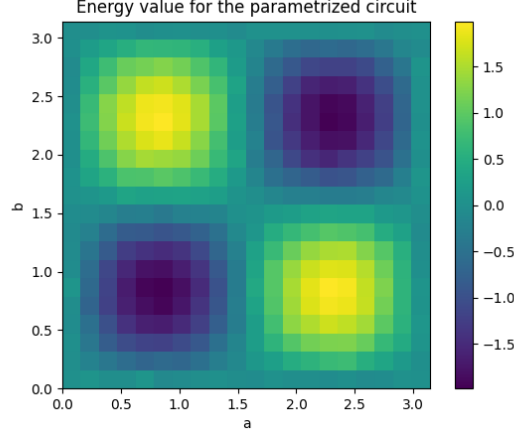
(a) Expectation value for the hamiltonian on the parameter space.
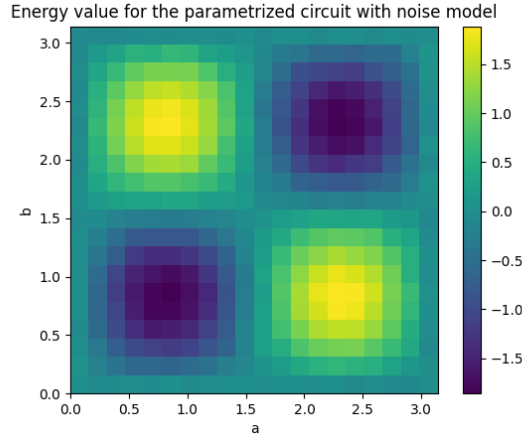
(b) Expectation value for the hamiltonian on the parameter space using a GAD noise model on all qubits on all four gates (p=0.2, $\gamma = 0.1$).

Figure 6.2: Energy landscape on the parameter space with and without noise.

The quantum state obtained when running the parametrized circuit with the optimal values is given up to a global phase by:

$$|\psi\rangle_{min} = \begin{pmatrix} 0.459 + i0.038 \\ 0.498 \\ 0.498 \\ -0.538 - i0.045 \end{pmatrix} \approx \frac{1}{2} \begin{pmatrix} 1 \\ 1 \\ 1 \\ -1 \end{pmatrix} = \frac{1}{\sqrt{2}}(|1-\rangle + |0+\rangle) \tag{6.4}$$

We check our results by applying the hamiltonian on the state:

$$\hat{H}|\psi\rangle = (-\hat{\sigma}_x^1\hat{\sigma}_z^2 - \hat{\sigma}_z^1\hat{\sigma}_x^2)\frac{1}{\sqrt{2}}(|1-\rangle + |0+\rangle) = -2\frac{1}{\sqrt{2}}(|1-\rangle + |0+\rangle) \tag{6.5}$$

We see that the results obtained are close to the theoretical ground state and minimum energy.For the energy we obtained a relative error of $\Delta E_{min} = 0.5\%$.

Another advantage of the VQE is that it is insensitive to homogeneous noise in first order. This is because the error gets taken into account into the optimization part of the algorithm. To test this we ran the same optimization with an amplitude damping noise model with $p = 0.2$ and $\gamma = 0.1$ [1]. The energy landscape turns more asymmetrical with the noise, as can be seen in Figure 6.2b. While the minimum energy value changes to $E_{min} = -1.15$ representing a high relative error of $\Delta E_{min} = 42\%$, the simulated ground state stays close to the ideal ground state. As we explained before, this is because the amplitude damping noise changes the total value of the expectation values but not the landscape of the parameter, leaving the values for a_{opt} and b_{opt} unchanged.

$$|\psi_{noise}\rangle_{min} = \begin{pmatrix} 0.459 + i0.116 \\ 0.499 \\ 0.499 \\ -0.509 + 0.129 \end{pmatrix} \tag{6.6}$$

7 Dynamical Quantum Phase Transitions

DQPTs extend the notion of phase transitions to the realm of non-equilibrium physics. For the more conventional equilibrium phase transitions, the central object is the partition function $Z = Tr(e^{-\beta \hat{H}(\alpha)})$ where β is an inverse temperature and the Hamiltonian depends on a set of parameters α. The partition function Z provides an implicit definition of a free energy density $f(\beta, \alpha)$ via $Z = e^{-\beta N f(\beta, \alpha)}$, which depends on both the inverse temperature and the parameters α.

Equilibrium phase transitions then occur at points where the free energy density $f(\beta, \alpha)$ becomes non-analytic as a function of either β or one of the parameters α. The former are temperature-driven phase transitions at some critical temperature T_c. The latter, if occurring at zero temperature, are called quantum phase transitions. In the context of DQPTs, we now instead consider the real-time evolution of a closed quantum many-body system starting from the ground state $|\psi_0\rangle$ of some Hamiltonian $\hat{H}_0$. At the time $t = 0$, the Hamiltonian is abruptly changed from $\hat{H}_0$ to $\hat{H}$, a protocol which is called a quantum quench. Formally, the time evolution is then solved by

$$|\psi_0(t)\rangle = e^{-i\hat{H}t} |\psi_0\rangle .$$

A formal similarity to the above partition functions is achieved by computing the return amplitude to the original ground state $|\psi_0\rangle$,

$$\mathcal{G}(t) = \langle \psi_0 | \psi_0(t) \rangle = \langle \psi_0 | e^{-i\hat{H}t} | \psi_0 \rangle ,$$

Which is called the Loschmidt amplitude. The associated return probability is called *Loschmidt echo*

$$\mathcal{L}(t) = |\mathcal{G}(t)|^2 = |\langle \psi_0 | \psi_0(t) \rangle|^2 . \tag{7.1}$$

For large N values they both take the following dependence on the system size:

$$\mathcal{G}(t) = e^{-Ng(t)} \tag{7.2}$$

$$\mathcal{L} = e^{-N\lambda(t)} \tag{7.3}$$

with g(t) being the associated rate function and $\lambda(t)$ the *Loschmidt rate*. These two rates are related by (Exercise 1):

$$\begin{aligned}
\mathcal{L}(t) &= |\mathcal{G}(t)|^2 \\
e^{-N\lambda(t)} &= |e^{-Ng(t)}|^2 \\
&= |e^{-N \, Re[g(t)]}|^2 \, |e^{Im[-Ng(t)]}|^2 \\
&= e^{2Re[-Ng(t)]} \cdot 1 \\
\lambda(t) &= 2Re[g(t)].
\end{aligned} \tag{7.4}$$

The exponential scaling with N shows a parallel with the exponential scaling of the state space with the number of particles. The expected overlap amplitude of two random states decays intuitively decreases with the dimensionality of the space they live in. If the quantum quench significantly changes the energy density of the system, the eigenstates of the Hamiltonian are expected to be very different, leading to the evolution of the original ground state of $|H_0\rangle$ into states that scarcely related. Therefore, the return amplitude is expected to decay with the dimensionality as long as the original eigenstate does not remain an eigenstate after the quench.

Equipped with these definitions, we identify DQPTs as points where both rates become non-analytic as a function of time. DQPTs occur at critical times t_c where the rates show a kink-like behavior in the thermodynamic limit ($N \longrightarrow \infty$). In the case that the initial Hamiltonian $\hat{H}_0$ has more than one ground state, i.e. in the presence of spontaneous symmetry breaking: ig i = 0, ..., N_{gs} labels all the ground states of the initial hamiltonian, the Loschmidt echo becomes:

$$\mathcal{L}(t) = \sum_l |\langle \psi_l | \psi_0(t) \rangle|^2 \tag{7.5}$$

And can be interpreted as the return probability to the ground state manifold of $\hat{H}_0$. We can also define the individual rates via $\lambda_l(t)$:

$$|\langle \psi_l | \psi_0(t) \rangle|^2 = e^{-N\lambda_l(t)} \tag{7.6}$$

In the large system limit ($N \to \infty$) it becomes apparent that the smallest of the individual Loschmidt rates is dominating (Exercise 2). We omit the explicit notation of time dependence for concision's sake.

$$
\begin{aligned}
lim_{N \to \infty}\mathcal{L} &= lim_{N \to \infty}\sum_l e^{-N\lambda_l} \\
&= lim_{N \to \infty}e^{-N\lambda_{min}}\sum_l e^{-N(\lambda_l - \lambda_{min})} \\
&= lim_{N \to \infty}e^{-N\lambda_{min}}(1 + \sum_{l \neq min} e^{-N\Delta\lambda_l}) \\
&= e^{-N\lambda_{min}}
\end{aligned}
\tag{7.7}
$$

where $\lambda_{min}(t) = min_l[\lambda_l(t)]$ describes the minimum function of all individual λ_l at each time step and $\Delta\lambda_l = \lambda_l - \lambda_{min}$. As long as there is a unique minimum of the set of individual Loschmidt rates, $\Delta\lambda_l$ is larger than 0 and the sum in 7.7 goes to 0 for large N. Therefore, the Loschmidt rate then reduces to $\lambda(t) = \lambda_{min}(t)$.

8 The Transverse Field Ising Model

$$\hat{H}(g) = -\frac{1}{2}\sum_{\langle l,j\rangle} Z_l Z_j - \frac{g}{2}\sum_l X_l \tag{8.1}$$

$$\hat{P} = \prod_k X_k \tag{8.2}$$

Each component of $\hat{P}$ acts on a separate subspace, so the overall eigenvalues are a product of the possible eigenvalues of the individual opearors (+1 and -1). The spectrum is therefore $+1, -1$ as well.

$$[\hat{H}, \hat{P}] = -\frac{1}{2}\sum_{\langle i,j\rangle}[Z_l Z_j, \hat{P}] - \frac{g}{2}\sum_l [X_l, \hat{P}] \tag{8.3}$$

Utilizing the linearity of the commutator, we split it into the two parts of the Hamiltonian and apply the rule that operators on different Subspaces (i.e. different particles with different indices) commute. The remaining part can be solved from the solution for multiplication of Pauli operators:

$$\sigma_l \sigma_j = -i\ \epsilon_{ljk}\ \sigma_k,$$

with $\sigma_1 = X, \sigma_2 = Y, \sigma_3 Z$. Applied to the operators at hand the following relations can be used:

$$X_k Z_j = i\delta_{jk}Y_j + (1 - \delta_{jk})Z_j X_k \tag{8.4}$$

and

$$Z_j X_k = -i\delta_{jk}Y_j + (1 - \delta_{jk})X_k Z_j. \tag{8.5}$$

With this, the commutation of the $\hat{H}$ and $\hat{P}$ is apparent:

$$\begin{aligned}
[Z_l Z_j, \hat{P}] &= Z_l Z_j \hat{P} - \hat{P} Z_l Z_j \\
&= (\prod_{k\neq i,j} X_k)(Z_l Z_j X_l X_j - X_l X_j Z_l Z_j) \\
&= (\prod_{k\neq i,j} X_k)\ i(Y_l Y_j - Y_l Y_j) \\
&= 0
\end{aligned} \tag{8.6}$$

$$\begin{aligned}
[X_l, \hat{P}] &= (\prod_{k\neq l} X_k)[X_l, X_l] \\
&= 0.
\end{aligned} \tag{8.7}$$

Exact ground states: g = 0

$$\hat{H}(g = 0) = -\frac{1}{2}\sum_{\langle l,j\rangle} Z_l Z_j \tag{8.8}$$

Minimum energy where $Z_l Z_j = 1 \quad \forall l, j$. This is achieved, if all spins are parallel, either in positive or negative Z direction. So the set of ground states is $\{|\psi_0\rangle = |0, 0, 0, ..., 0\rangle, |\psi_1\rangle = |1, 1, 1, ..., 1\rangle\}$. The symmetry of the two ground states is spontaneously broken for an infinitesimally small longitudinal field appearing as $\pm \epsilon \sum_l Z_l$ in the Hamiltonian. An energy gap of $2N\epsilon$ is introduced between $|\psi_0\rangle$ and $|\psi_1\rangle$ is introduced. The expectation value of the ground state magnetization $\langle m_z \rangle = \langle \psi_g | \frac{1}{N} \sum_l Z_l | \psi_g \rangle$ becomes ∓ 1, depending on the polarization of the the longitudinal field.

The other boundary case, for infinitely strong coupling to the transversal field, the ground state is a perfect alignment with the external field. The next-neighbor interaction in the Hamiltonian becomes negligible:

$$\hat{H}(g) \xrightarrow{g \to \infty} -\frac{g}{2} \sum_l X_l. \tag{8.9}$$

The ground state is the the the one that maximizes the expectation value of X for every particle. There is only one configuration, the non-degenerate ground state $|\psi_0\rangle = |+, +, +, ...\rangle$. The ground state of the system is completely demagnetized: $\langle m_z \rangle = 0$.

Applying the Kramers-Wannier transformation, we introduce the new Ising variables

$$\tilde{Z}_n = \prod_{l \leq n} X_l \tag{8.10}$$

$$\tilde{X}_n = Z_n Z_{n+1}. \tag{8.11}$$

By checking the anti-commutation relation of these new variables, we confirm that they qualify to replace the Pauli Operators (Exercise 4).

$$
\begin{aligned}
\{\tilde{Z}_n, \tilde{X}_n\} &= Z_n Z_{n+1}(\prod_{l \leq n} X_l) + (\prod_{l \leq n} X_l) Z_n Z_{n+1} \\
&= (\prod_{l < n} X_l) Z_n X_n Z_{n+1} + (\prod_{l < n} X_l) X_n Z_n Z_{n+1} \\
&= (\prod_{l < n} X_l) i(Y_n - Y_n) Z_{n+1} \text{ (with 8.4 and 8.5)} \\
&= 0
\end{aligned}
\tag{8.12}
$$

Considering that $X_l X_l = \mathbb{I}$, we see that X_n corresponds to $\tilde{Z}_{n-1}\tilde{Z}_n$. Furthermore, for a 1-D lattice where every node is bound to the node before and after, $\sum_{\langle l,j \rangle} Z_l Z_j = \sum_{\langle n,n+1 \rangle} \tilde{X}_n$. In this case the summation over all neighboring sites n and l $\langle n, l \rangle$ is equivalent to the summation over all n and setting $l = n - 1$, up to boundary terms. So the Hamiltonian can be expressed as

$$\tilde{H} = -\frac{1}{2} \sum_n \tilde{X}_n - \frac{g}{2} \sum_{\langle n,l \rangle} \tilde{Z}_n \tilde{Z}_l \tag{8.13}$$

This is the exact same form as the original Hamiltonian (8.1), up to the exchange of the prefactors. Hence, we can conclude that the new Ising variables correspond to a switched assignment of the ground states, because the dominating term with respect to the magnitude of g is inverted. At the critical point, the ferromagnetic state and the paramagnetic state have the same energy in both formulations of the Hamiltonian have to be the same, which is the case when g assumes the value $g_c = 1$.

For couplings to the transversal field, that are lower than 1, a ferromagnetic ordering of the ground state is expected when no temperature is regarded. The energy difference between the ground state and a state with two domains amounts to a constant term of $\frac{1}{2}$ in the units of the Hamiltonian. This does not scale with the system size, because the

Ising model only takes into account nearest neighbor interactions. Domain walls can occur between all neighboring particles, so the state space D_2 for two domains contains $N - 1$ (i.e. $\mathcal{O}(N)$) states, for three D_3 domains scales with $(N-1)(N-2)$ ($\mathcal{O}(N^2)$) etc.

The thermal state of the system is given by the equilibrium density matrix $\rho = \frac{e^{\hat{H}'/kT}}{Z}$ with $Z = Tr[e^{\hat{H}'/kT}]$ [[2]]. With the normalized $\hat{H}' = \hat{H} - \langle\psi_g| \hat{H} |\psi_g\rangle$, we find that Z scales

$$
\begin{aligned}
Z &= e^0 + \sum_{\psi \in D_2} e^{-\langle\psi_k|\hat{H}|\psi_k\rangle/kT} + \sum_{\psi \in D_3} e^{-\langle\psi_k|\hat{H}|\psi_k\rangle/kT} + \dots \\
&> 1 + (N-1)e^{-1/kT} + (N-1)(N-2)e^{-2/kT}
\end{aligned}
\tag{8.14}
$$

For large systems, the probability to find the ground state $\langle\psi_g| \rho |\psi_g\rangle = \frac{1}{Z}$ decays to 0 for finite temperatures and large system sizes N. A long range ferromagnetic order will therefore not be observed in an Ising chain.

9 DQPTS in the TFI

For the simulation of time evolution for the transverse field ising model on qiskit we perform a Trotter decomposition of the the unitary operator $U(t) = e^{-i\hat{H}t}$ with the hamiltonian in Equation 8.1. As a first step we rewrite

$$U(t) = e^{-i\hat{H}t} = (e^{-i\hat{H}dt})^{\frac{t}{dt}} = (e^{\hat{A}+\hat{B}})^{\frac{t}{dt}},$$

with $\hat{A} = idt\frac{g}{2}\sum_i X_i$, and $\hat{B} = idt\frac{1}{2}\sum_{\langle i,j\rangle} Z_i Z_j$.

On the first order approximation for the Trotterization we have:

$$e^{\hat{A}+\hat{B}} \approx e^A e^B \tag{9.1}$$

The second order Trotterization is given by:

$$e^{\hat{A}+\hat{B}} \approx e^{A/2} e^B e^{A/2} \tag{9.2}$$

In the approximation the system is evolved in small time steps given by dt, so smaller values of dt should yield better approximations.
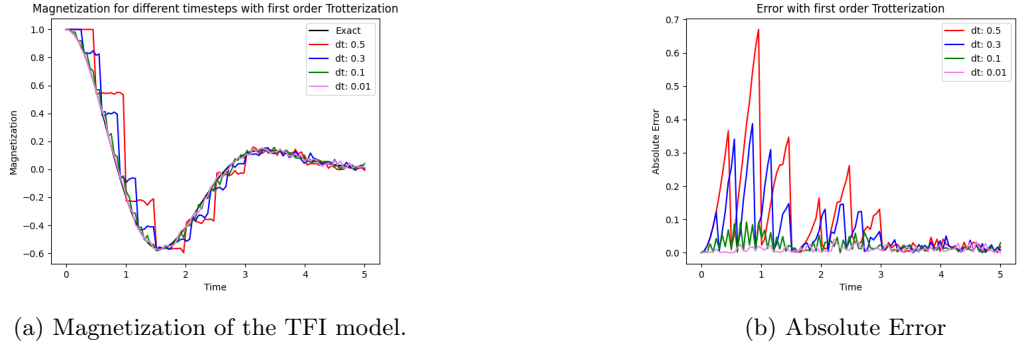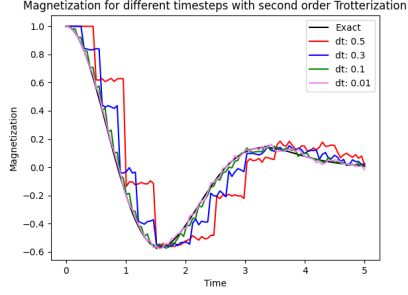

(a) Magnetization of the TFI model.

(b) Absolute Error

Figure 9.1: Magnetization of TFI model simulated with first order Troterization with 10 qubits and g=2. for different timesteps

As expected, Figure 9.1 shows better approximation for smaller values of dt. With $dt = 0.5$, the error is too high for the simulation to be useful. However, at $dt = 0.1$, the results dramatically improve, and with $dt = 0.01$, the curves of the simulation and the exact results are almost indistinguishable for most of the time evolution. It is important to note, however, that lower values of dt significantly increase the time required for the simulation.

The second-order approximation results shown in Figure 9.2 have a similar behaviour for smaller values ($dt = 0.01$ and $dt = 0.1$), the results were slightly better than the first-order approximation.

Having implemented the time evolution simulation we can now evaluate the Loschmidt rate as described in Chapter 7. The initial hamiltonian is chosen as $\hat{H}(g=0) = -\frac{1}{2}\sum Z_l Z_j$, where the two degenerate ferromagnetic ground states are $|\psi_0\rangle = |0...0\rangle$ and $|\psi_1\rangle = |1...1\rangle$.

(a) Magnetization of the TFI model.
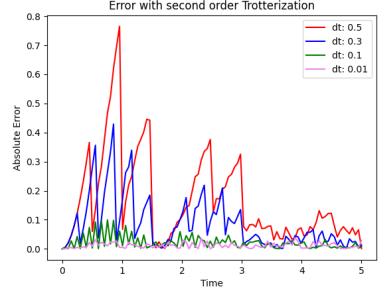
(b) Absolute Error

Figure 9.2: Magnetization of TFI model simulated with second order Troterization with 10 qubits and g=2. for different timesteps
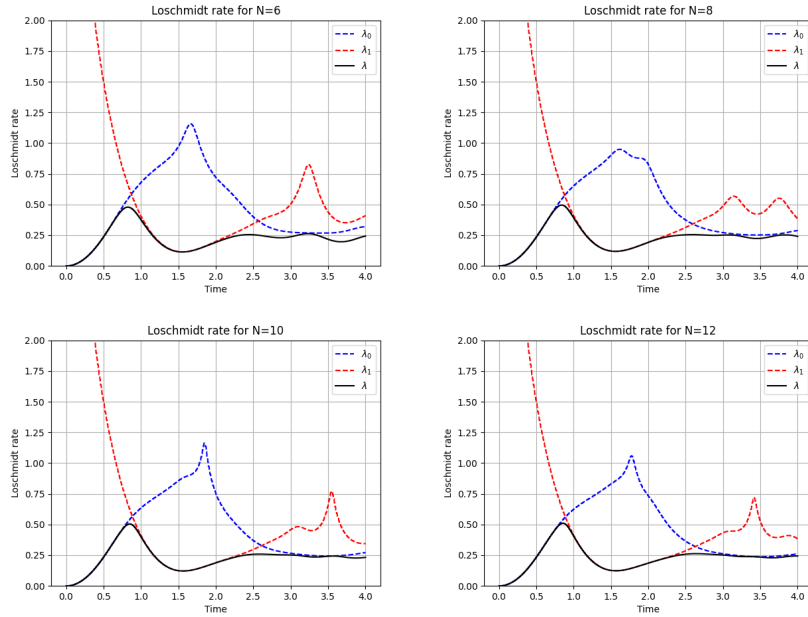

Figure 9.3: Simulated Loschmidt rate and individual Loschmidt rates as a function of time with g=2 using a timestep of dt=0.01 for different system sizes N

From Figure 9.3 we can see that even for the smallest system simulated (N=6) the general Loschmidt rate takes the value of the smallest individual rate during the simulation, as showed in Chapter 7. We can also identify the DQPTs in the graph at the *critical times* t_c where the rates behave non-analytical shown on the kink-like behaviour of the plots.
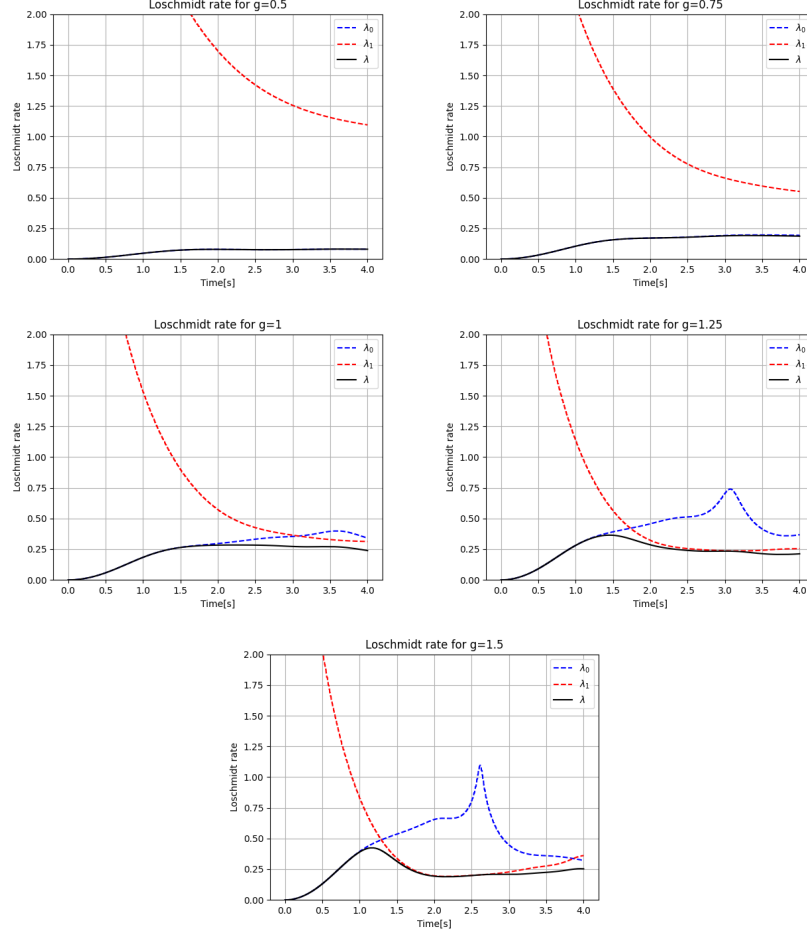

Figure 9.4: Simulated Loschmidt rate and individual Loschmidt rates as a function of time with N=8 using a timestep of dt=0.01 for different values of g.

In Figure 9.4, we can see that for the first three values of $g \in [0.5, 0.75, 1]$, no DQPTs are present. For the two biggest values of $g = 1.25$ and $g = 1.5$, a DQPT form for the individual rate λ_0 at times 3.1s and 2.6s respectively.

To better resemble how actual experiments on quantum computers work, we will not work with the state vector of the exact time-evolved wave function. Instead, we will **measure** and average over all the measurements to calculate the expectation values and overlaps for the magnetization and Loschmidt rate, respectively. We ran the simulations with increasing measurements or shots to determine at which number one gets accurate results.

From Figure 9.5, we see that with 1000 shots, we already get accurate results for the magnetization, whereas, for the Loschmidt rate, 5000 shots are required to get results of similar quality.

When plotting the magnetization and the Loschmidt rate on the same graph, one sees that they start at 1 and 0, respectively; this makes sense as the initial state is $|\psi\rangle = |0\rangle^N$ which is the maximum magnetization state, and has zero overlaps with the other ground
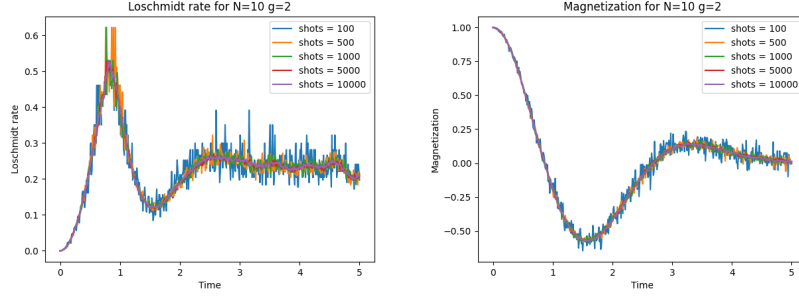
Figure 9.5: Loschmidt rate and magnetization obtained with sampled measurements for N=10, g=2 and dt=0.01 for different number of shots $S \in [100, 500, 1000, 5000, 10000]$.
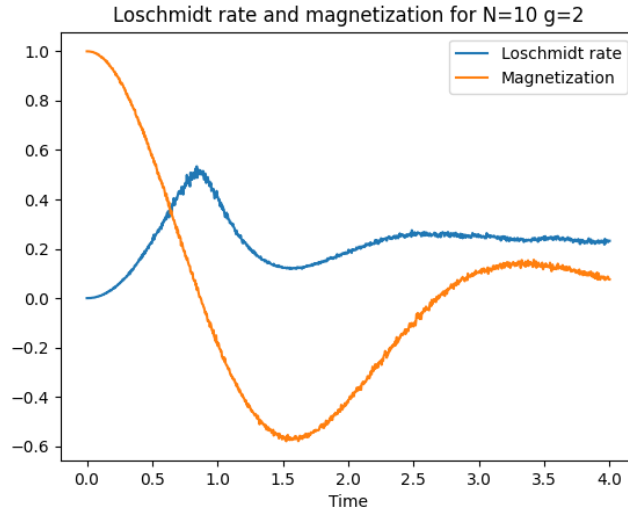

Figure 9.6: Comparison of the Loschmidt rate and magnetization.

state $|1\rangle^N$ which is why the Loschmidt rate is equal to 0. Afterward, the state evolves, which makes the overlap with $|1\rangle^N$ increase until the Loschmidt rate reaches a maximum and the magnetization keeps decreasing, however when the overlap for the $|0\rangle^N$ state decreases too much the Loschmidt rate starts decreasing again. The magnetization keeps decreasing until reaching a local minimum at the point in the time evolution where the overlap with the $|1\rangle^N$ reaches its maximum.

Tracking the entanglement production

The time evolution after a quantum quench generates entanglement in the system, which can be quantified using the half-chain entropy derived from the reduced density matrix of one half of the quantum chain

$$\rho_l = \text{Tr}_r[\rho], \tag{9.3}$$

where ρ is the density matrix of the complete system. Two measures of entanglement are considered, the von Neumann entropy

$$S = -\text{Tr}[\rho_l \log(\rho_l)], \tag{9.4}$$

and the second Rényi entropy

$$S^{(2)} = -\log\left(\text{Tr}[\rho_l^2]\right). \tag{9.5}$$

25

The density matrix ρ of the entire system can be determined by State Tomography. Since the quantum computer only performs population measurements (z-components), additional rotations U_j ($j \in \{1, \ldots, 3^N\}$) are applied to access other components. For N qubits, the probabilities p_{jk} for all basis states $|k\rangle$ ($k = 1, \ldots, 2^N$) are measured, and the density matrix is reconstructed via linear inversion:

$$p_{jk} = \langle k | U_j^\dagger \rho U_j | k \rangle. \tag{9.6}$$

Next, we investigate the findings on the entanglement build-up following the quantum quench. Simulations reveal a growth in entanglement, as shown in Figure 9.7, which depicts the time evolution of the von Neumann and second Rényi half-chain entropies (Equations 9.4 and 9.5). Initially, entropy remains constant but later increases, with early fluctuations giving way to linear growth. The second Rényi entropy grows more slowly than the von Neumann entropy.
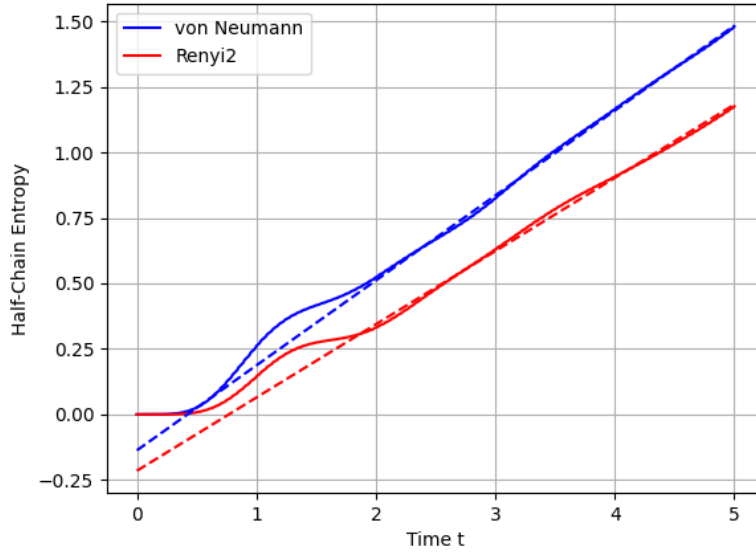

Figure 9.7: Simulated time evolution of the von Neumann and second Rényi half-chain entropies after the quantum quench: At larger times, both entropies exhibit linear growth, while at smaller times, deviations from linearity are observed.

Measurements on a quantum computer verify these simulations. Using State Tomography (Section 5), the density matrix is reconstructed at each time step, and entropies are computed after a partial trace. Figure 9.8 shows that the measured entropy slightly overestimates the simulation, particularly for the von Neumann entropy. The results are limited to small systems because of computational constraints.
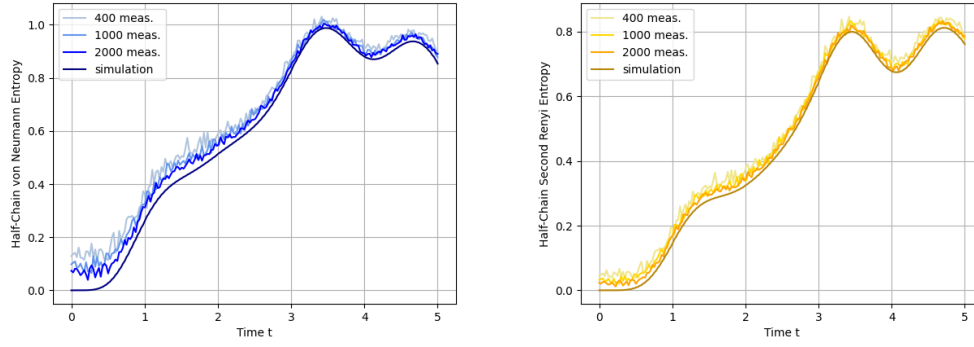
Figure 9.8: Measurement results for the half-chain von Neumann and second Rényi entropies obtained via State Tomography, with $L = 4$ and $dt = 0.01$: The measured values align closely with the simulations. Increasing the number of measurements per time step enhances precision and reduces fluctuations. However, the State Tomography method slightly overestimates the entropies.

References

[1] Qiskit. Amplitude damping error function, 2024.

[2] Manirul Ali, Wei-Ming Huang, and Wei-Min Zhang. Quantum thermodynamics of single particle systems. *Scientific Reports*, 2020.